SCIENCE CHINA
Chemistry

•ARTICLES•

March 2018 Vol.61 No. 3: 344–350
https://doi.org/10.1007/s11426-017-9174-9

Hierarchically nanostructured porous TiO_2(B) with superior photocatalytic CO_2 reduction activity

Tingmin Di[1], Jinfeng Zhang[1], Bei Cheng[1], Jiaguo Yu[1,2*] & Jingsan Xu[3*]

[1] *State Key Laboratory of Advanced Technology for Materials Synthesis and Processing, Wuhan University of Technology, Wuhan 430070, China;*
[2] *Department of Physics, Faculty of Science, King Abdulaziz University, Jeddah 21589, Saudi Arabia;*
[3] *School of Chemistry, Physics and Mechanical Engineering, Queensland University of Technology, Brisbane QLD 4001, Australia*

Received October 4, 2017; accepted November 7, 2017; published online January 25, 2018

Hierarchically nanostructured, porous TiO_2(B) microspheres were synthesized by a microwave-assisted solvothermal method combined with subsequent heat treatment in air. The materials were carefully characterized by scanning and transmission electron microscopy, X-ray diffraction, CO_2 adsorption, and a range of spectroscopies, including Raman, infrared, X-ray photoelectron and UV-Vis spectroscopy. The hierarchical TiO_2(B) particles are constructed by ultrathin nanosheets and possess large specific surface area, which provided many active sites for CO_2 adsorption as well as CO_2 conversion. The TiO_2(B) nanostructures exhibited marked photocatalytic activity for CO_2 reduction to methane and methanol. Anatase TiO_2 and P25 were used as the reference photocatalysts. Transient photocurrent measurement also proved the higher photoactivity of TiO_2(B) than that of anatase TiO_2. *In-situ* infrared spectrum was measured to identify the intermediates and deduce the conversion process of CO_2 under illumination over TiO_2(B) photocatalyst.

photocatalytic CO_2 reduction, TiO_2(B), hierarchical nanostructure, anatase TiO_2

Citation: Di T, Zhang J, Cheng B, Yu J, Xu J. Hierarchically nanostructured porous TiO_2(B) with superior photocatalytic CO_2 reduction activity. *Sci China Chem*, 2018, 61: 344–350, https://doi.org/10.1007/s11426-017-9174-9

1 Introduction

The approach that utilizes natural solar energy with the assistance of photocatalysts for converting carbon dioxide (CO_2) into renewable hydrocarbon fuels such as methane (CH_4) and methanol (CH_3OH) is believed to be a promising way for reducing the CO_2 levels in the atmosphere [1–3]. This photocatalytic technique could simultaneously tackle the greenhouse effect caused by the rising atmospheric levels of CO_2 and the depletion of fossil fuels [4–9]. Since the pioneering work reported by Inoue *et al*. [10] that CO_2 can be reduced to HCOOH and CH_3OH over semiconductors under light irradiation, numerous photocatalysts have been employed to investigate photocatalytic CO_2 reduction [11–13]. Among various semiconductors used for photochemical reduction of CO_2, TiO_2 has been extensively studied for its remarkable photocatalytic performance, low cost, good photo-stability, and low toxicity features [8,14–18]. It is well recognized that the phase structure of a semiconductor significantly affects its physical and chemical properties, and hence determines the photocatalytic performance [19,20]. In general, TiO_2 has four polymorphs including anatase (tetragonal), rutile (tetragonal), brookite (orthorhombic) and TiO_2 (B) (monoclinic). Among them, anatase and rutile are the most investigated two polymorphs for their excellent photocatalytic activity and high stability [21]. In addition, it has been reported that TiO_2(B) is metastable and possesses a

---

*Corresponding authors (email: yujiaguo93@yahoo.com; Jingsan.Xu@qut.edu.au)

© Science China Press and Springer-Verlag GmbH Germany 2018

more negative conduction band (CB) edge than anatase, which thermodynamically endows its conduction electrons strong reduction capability upon photoexcitation [22,23]. However, comparing with the other three allotropes of TiO_2, monoclinic TiO_2(B) has been rarely studied for photocatalysis; instead, it attracts significant interest as an anode material for lithium-ion batteries [24–28]. In particular, to the best of our knowledge, there has been no report on the photocatalytic activity of TiO_2(B) for CO_2 reduction.

Besides phase structures, crystal morphology is another critical factor affecting the photocatalytic properties of semiconductors [29–33]. The self-assembly synthesis of hierarchical nanostructures is a feasible strategy to enhance the surficial adsorption of reactants and facilitate the transport of guest species. Nanosheet-constructed TiO_2(B) microparticles by microwave-solvothermal reaction have been prepared with the assistance of the ionic liquid ([bmin][BF_4]) on the basis of hydrolysis of $TiCl_3$ in ethylene glycol (EG) [34]. However, a lot of residual organics existed in the as-formed TiO_2(B) nanosheets. Moreover, the photocatalytic activities of the obtained TiO_2 material, especially its activity for photocatalytic CO_2 reduction, was not investigated.

Herein, porous hierarchical TiO_2(B) particles were synthesized by a modified microwave assisted solvothermal method, following by calcination at 350 °C in air to remove the residual organics and improve the crystallinity of TiO_2 (B). Another TiO_2 sample was prepared by calcination at 650 °C in air to transform the TiO_2(B) to anatase TiO_2 (donated as TiO_2(A)). In this work, commercial P25 (a mixture of anatase and rutile TiO_2) and TiO_2(A) were used as reference photocatalysts for the evaluation of photocatalytic CO_2 reduction over the as-obtained TiO_2(B).

2 Experimental

2.1 Sample preparation

Firstly, the TiO_2 precursor was synthesized using a microwave-assisted solvothermal method. In a typical synthetic process, 0.2 mL [Bmim][BF_4] were added into 15 mL ethylene glycol (EG) and 1 mL deionized water mixture solution, then 1 mL $TiCl_3$ (15 wt% in diluted HCl) were mixed with the above solution. The homogeneous mixture was then transferred into a Teflon-lined autoclave, which was placed in a microwave-hydrothermal synthesis system (MDS-6, Sineo, China) and kept at 180 °C for 60 min. After the reaction, the white precipitate was collected by centrifugation, rinsed several times with distilled water and then dried in an oven at 80 °C for over 12 h. In order to remove the surface adsorbed organics and enhance the crystallinity of TiO_2(B), the precursor was calcined in a muffle at 350 °C for 2 h. For comparison, another sample was prepared by a similar strategy with the calcination treatment at 650 °C for 2 h to transform the TiO_2(B) to anatase TiO_2 (donate as TiO_2(A)).

2.2 Characterization

Rigaku X-ray diffractometer (Japan) with Cu Kα radiation was used to test X-ray diffraction (XRD) patterns. Morphological observations were conducted on a JEOL JSM-7500 field emission scanning electron microscope (FESEM, Japan) and JEOL JEM-2100F transmission electron microscope (TEM, Japan). Thermogravimetric-differential thermal analysis (TG-DTA) was performed on a thermal analyzer (DTG-60, Shimadzu, Japan) under ambient atmospheric with a temperature ramp of 3 °C min^{-1}. The X-ray photoelectron spectroscopy (XPS) was measured on a Thermo ESCALA 250 XPS spectrometer system with Al Kα (1486.6 eV) radiation (USA). The binding energies were referenced to the C 1s peak at 284.8 eV from adventitious carbon. The Brunauer-Emmett-Teller (BET) specific surface area (S_{BET}) of the powders was measured on a Micromeritics ASAP 2020 with nitrogen adsorption apparatus. CO_2 adsorption was measured using an ASAP 3020 carbon dioxide adsorption apparatus (Micromeritics, USA). UV-Vis diffuse reflectance spectra were analyzed on a Shimadzu UV-2600 UV-Vis spectrophotometer (Japan). Electrochemical measurements were implemented on electrochemical analyzer (CHI660C, China) in a standard three-electrode system with the as-prepared samples as the working electrode, a Pt wire as the counter electrode and Ag/AgCl (saturated KCl) as a reference electrode. A 365 nm LED-light was utilized as the light source. Na_2SO_4 (0.5 M) aqueous solution was used as the electrolyte. The working electrodes were prepared as follows: 0.05 g of photocatalyst was ground with 0.5 mL of ethanol to make a slurry. The slurry was then coated onto a 2 cm×1.2 cm F-doped SnO_2-coated glass (FTO glass) electrode by the doctor blade technique. Next, these electrodes were dried in an oven at 80 °C for 30 min. The electrodes have film thickness of ca. 10 μm.

2.3 Photocatalytic reduction of CO_2

The photocatalytic reduction of CO_2 was operated in a 200 mL homemade Pyrex reactor at an ambient temperature and atmospheric pressure, similar to that reported in our previous study [35]. Typically, 100 mg of catalyst was evenly coated as a thin film on the bottom of the reactor by evaporating a catalyst-containing aqueous suspension to dryness at 80 °C for 3 h. Before irradiation, the reactor was sealed and blown with nitrogen for 30 min to keep an anaerobic condition. CO_2 and H_2O sources were introduced by reaction of $NaHCO_3$ (84 mg, added into the reactor before seal) and H_2SO_4 aqueous solution (0.3 mL, 2 M, syringed into the reactor after N_2 blowing). A 300 W Xe light was positioned 20 cm vertically above the photocatalytic reactor as light source. Gas product (1 mL, taken from the reactor) was analyzed using a gas chromatograph (GC-2014C, Shimadzu, Japan) equipped with a flame ionized detector (FID) and methanizer. The reduced products in this experiment were calibrated with a standard gas mixture and determined from the retention time. $^{13}CO_2$ isotope tracer experiment was conducted to verify the carbon resource.

$^{13}CO_2$ isotope tracer experiment was conducted to verify the carbon source of the products by using ^{13}C isotope-labelled sodium bicarbonate ($NaH^{13}CO_3$, Cambridge Isotope Laboratories Inc., USA) and H_2SO_4 aqueous solution for the photocatalysis examinations. After 1 h of photocatalytic reaction, 250 μL of mixed gas was taken out from the reactor and examined by a gas chromatography-mass spectrometer (GC-MS) (6980N network GC system-5975 inert mass selective detector, Agilent technologies, USA) to analyze the products.

2.4 *In-situ* FTIR for CO_2 adsorption and conversion

Nicolet is 50 spectrometer (Thermo fisher, USA) was used to record the *in-situ* Fourier transform infrared (FTIR) spectra. Before measuring FTIR spectra, the photocatalysts have been treated at 150 °C on Micromeritics ASAP 2020 to desorb the surface adsorbed molecules. The *in-situ* FTIR analysis was carried out in two sequential steps, similar to our previously reported literature [36,37]. Firstly, CO_2 adsorption on the surface of the sample was carried out 1 h in the dark with the continuous flow of a mixture of CO_2 and H_2O vapor (CO_2 was continuously passed through a water bubble into the chamber). And then, a LED light of 365 nm was turned on and illuminated for 1 h to investigate the conversion of the intermediates formed in the first step. It should be noted that IR spectrum of the photocatalyst was firstly collected as the background prior to CO_2 adsorption. When introducing the CO_2 onto the photocatalyst, IR spectra of the adsorbed species were obtained by subtracting the background.

3 Results and discussion

3.1 Morphology, structure and composition

Figure 1 shows the morphological results of TiO_2(B) obtained by heating the precursors at 350 °C. As can be seen from the FESEM images (Figures 1(a, b)), the TiO_2(B) is composed of hierarchically nanostructured microspheres assembled by nanosheets. The nanosheets have thicknesses of ~30 nm and their packing in three dimensions results in porous structures. Figure 1(c) shows the TEM picture of the individual TiO_2(B) particle, which confirms the nanosheets-constructed hierarchical structure of the TiO_2(B) microspheres. The HRTEM image (Figure 1(d)) displays one nanosheet and demonstrates its high crystallinity. It shows lattice fringes with spacing of 0.62 and 0.35 nm, which correspond to the (001) and (110) crystal plane of TiO_2(B), respectively, suggesting that the nanosheets growing along the *ab* plane.

Moreover, we found that there was a morphological evolution for the TiO_2 precursor during heating at various elevated temperatures. As can be seen from Figure 2, the precursor obtained by the hydrothermal process consisted of microspheres with well-defined, smooth nanosheets with sharp edges. After heating at 250, 350 and 450 °C in air, the microspheres shrunk somehow and meanwhile, the nanosheets bent a bit, owing to the release of organic species and the resulted stress. With further increased the temperature to 550 and 650 °C, nevertheless, we observed that the nanosheets reconstructed and become straight again. We consider that this morphological reconstruction should be associated with phase transition of the precursor during heat treatment.

Figure 3(a) presents the thermogravimetric-differential thermal analysis of the TiO_2 precursor ranging from 30 to

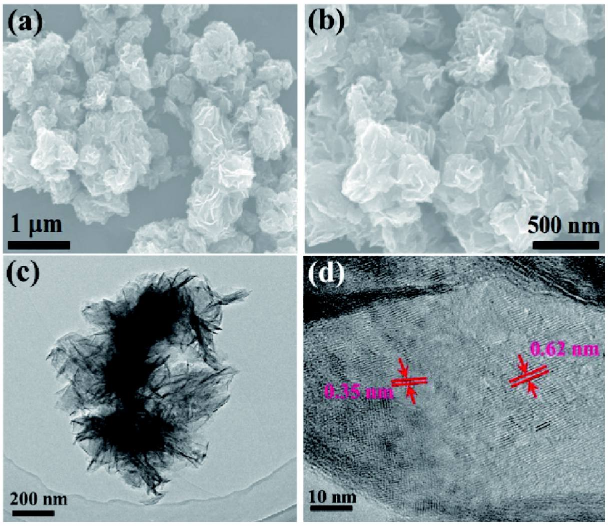

Figure 1 FESEM images (a, b), TEM (c) and HRTEM (d) images of porous hierarchical TiO_2(B) particles (color online).

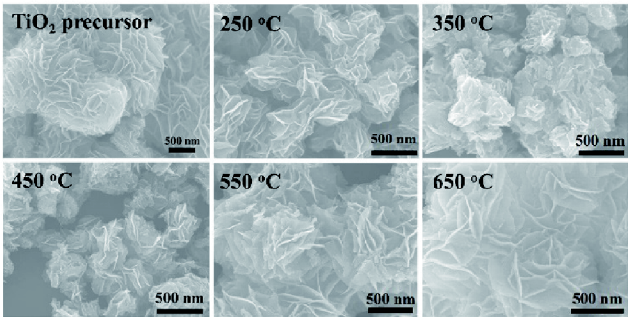

Figure 2 FESEM pictures of the TiO_2 precursor and the products obtained after heat treatment at different temperatures.

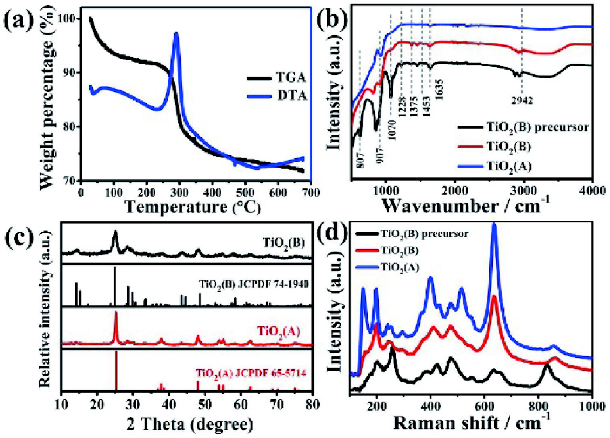

Figure 3 (a) TG-DTA curves of the TiO_2 precursor in air; (b) FTIR spectra of the TiO_2 precursor, TiO_2(B) and TiO_2(A); (c) XRD pattern of the TiO_2(B) and TiO_2(A) and corresponding PDF standard cards; (d) Raman spectra of the TiO_2 precursor, TiO_2(B) and TiO_2(A) (color online).

700 °C in air. There is a significant weight loss from ca. 250 to 340 °C, arising from the combustion of the residual organics from the hydrothermal process. When the temperature is higher than 340 °C, the weight turned to be stable, indicating that annealing at 350 °C in air can effectively remove the contained organic species. Therefore, we annealed the hydrothermal product at 350 °C in air to prepare the TiO_2 (B) sample for characterization and performance test. Figure 3(b) shows the FTIR spectra of the typical samples. We can see that the as-prepared TiO_2 precursor shows strong adsorption peaks at 807, 907 and 1070 cm^{-1}, which are assigned to the vibration mode of C–H plane vibration, –OH bending vibration and C–O asymmetric deformation, respectively. These vibration modes arise from the residual EG molecule attached in the TiO_2 precursor. After annealing at 350 and 650 °C, these vibration peaks significantly decreased or completely vanished, suggesting the removal of the residual organic components.

XRD was carried out to investigate the phase structure of the prepared samples. As shown in Figure 3(c), the XRD pattern of the TiO_2(B) matches well with monoclinic polymorph TiO_2(B) (JCPDS NO. 74-1940). As expected, the sample annealed at 650 °C shows improved crystallinity and most of the diffraction peaks are assigned to anatase TiO_2 (JCPDS NO. 65-5714). This phase transition was further confirmed by Raman spectroscopy. As shown in Figure 3(d), the characteristic peak of anatase at 148 cm^{-1} appeared in the Raman shift for the TiO_2(A) sample, which agrees well with the XRD result. XPS was employed to investigate the surface chemical states of the resulting TiO_2(B) and TiO_2(A) products. The XPS survey spectra in Figure 4(a) shows that only Ti, O and C elements were detected for both TiO_2(B) and TiO_2(A), suggesting that the [bmin][BF_4] used in the reaction was effectively removed. As shown in Figure 4(b), the Ti 2p high-resolution spectra of TiO_2(B) and TiO_2(A) are very close, suggesting the similar bonding environment of Ti atoms in the two samples. The two peaks of Ti $2p_{3/2}$ at 458.5 eV and Ti $2p_{1/2}$ at 464.2 eV are assigned to the characteristic peaks of Ti^{4+} in TiO_2. The O 1s spectra (Figure 4(c)) of both TiO_2(B) and TiO_2(A) were deconvoluted to two peaks of surface lattice oxygen (at 529.8 eV) and surface Ti–OH groups (at 531.1 eV). TiO_2(B) and TiO_2(A) display almost the same peak positions for both Ti 2p and O 1s high-resolution spectra.

3.2 Surface areas and pore size distributions

N_2 adsorption-desorption were measured and recorded to investigate the specific surface area (S_{BET}) and porosity of the samples. As shown in Figure 4(d), both TiO_2(B) and TiO_2(A) have isotherms of type IV and hysteresis loops of type H3 at higher relative pressure (P/P_0) range of 0.8–1.0, indicating the presence of slit-like pores [38–40]. Furthermore, the isotherm of sample TiO_2(B) shifts up compared with TiO_2(A) at the low P/P_0 range (<0.2), indicating TiO_2(B) has a higher S_{BET} than TiO_2(A), as shown in Table 1. Besides, TiO_2(B) shows a broad pore size distribution than TiO_2(A), as indicated in the inset of Figure 4(d), probably owing to the growth and reconstruction of the nanoparticles during the treatment at elevated temperature.

3.3 Band structures

The UV-Vis reflectance spectra (Figure 4(e)) of the TiO_2 samples measured and recorded, with TiO_2(B) and TiO_2(A) showing very similar curves. The bandgap of TiO_2(B) and TiO_2(A) was determined to be 3.34 and 3.23 eV, respectively. Moreover, Mott-Schottky measurement was carried out to investigate the band structures. As shown in Figure 4(f), the flat-band potential (E_{fb}) of the TiO_2(B) was determined to be –0.74 V by extrapolation of the X intercepts in Mott-Schottky plot, which is more negative than the potential of –0.68 V for TiO_2(A). The more negative E_{fb} endows thermodynamically stronger reduction ability of the TiO_2(B) conduction electrons than TiO_2(A), which is beneficial to CO_2 conversion.

3.4 CO_2 adsorption and photocatalytic CO_2 reduction

The CO_2 adsorption onto the photocatalyst is the first step that critically affects the photocatalytic conversion of CO_2 to hydrocarbons. Figure 5(a) displays the CO_2 adsorption isotherms of the samples, exhibiting that TiO_2(B) has an adsorption amount of 0.42 mmol g^{-1}, while the adsorption amount of TiO_2(A) is only 0.24 mmol g^{-1}, mainly resulting from the higher surface area of TiO_2(B). In the photocatalytic CO_2 reduction measurements, control experiments were carefully conducted in the absence of photocatalysts, irra-

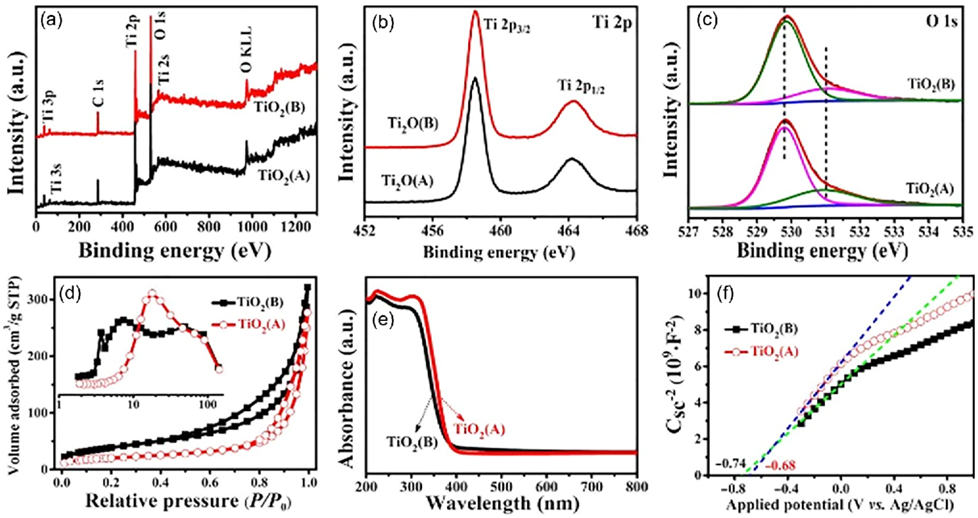

Figure 4 XPS survey spectra (a), high-resolution X-ray photoelectron spectra of Ti 2p (b) and O 1s (c); nitrogen adsorption-desorption isotherms and the corresponding pore-size distribution curves (inset) (d), UV-Vis diffuse reflection spectra (e), Mott-Schottky plots (f) of TiO_2(B) and TiO_2(A) (color online).

Table 1 Specific surface area, pore volume, pore diameter and the corresponding CO_2 uptake ability of TiO_2(B) and TiO_2(A)$^{a)}$

Sample	CT (°C)	S_{BET} ($m^2\ g^{-1}$)	PV ($cm^3\ g^{-1}$)	APS (nm)	CA ($mmol\ g^{-1}$)
TiO_2(B)	350	142	0.34	9.5	0.42
TiO_2(A)	650	73	0.28	15.2	0.25

a) CT: calcined tempreature; PV: pore volume; APS: average pore size; CA: CO_2 adsorption quantity corresponding to a P/P_0 of 1.0

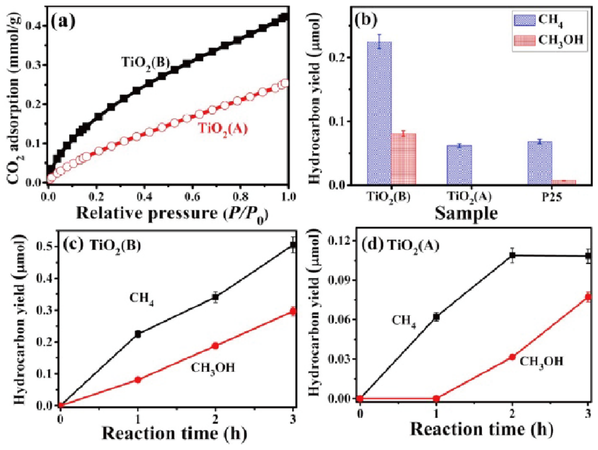

Figure 5 (a) CO_2 adsorption curves of TiO_2(B) and TiO_2(A); (b) CH_4 and CH_3OH generated after the first-hour illumination upon TiO_2(B), TiO_2(A) and P25. Time courses of photocatalytic CH_4 and CH_3OH production over TiO_2(B) (c) and TiO_2(A) (d) (color online).

diation, H_2O or carbon source (using N_2 as the carrier gas). We found that hydrocarbons emerged only in the presence of the photocatalysts, irradiation, H_2O and CO_2, confirming that the hydrocarbons resulted exclusively from the photocatalytic CO_2 reduction. Figure 5(b) presents the yield of CH_4 and CH_3OH after 1 h illumination over TiO_2(B), TiO_2(A) and P25, respectively. TiO_2(B) shows much higher hydrocarbons yield than TiO_2(A) and P25, with the CH_4 yield of 0.23 μmol and CH_3OH yield of 0.08 μmol. Figures 5(c, d) show the time courses of photocatalytic CH_4 and CH_3OH generation over TiO_2(B) and TiO_2(A), respectively. Continuous increases of CH_4 and CH_3OH amount for both TiO_2(B) could be observed upon up to 3 h illumination. Meanwhile, their production rates were higher over TiO_2(B) than over TiO_2 (A). These results clearly indicate that TiO_2(B) exhibits better photocatalytic CO_2 reduction performance than TiO_2 (A), which should result from the higher surface area, more negative conduction band and the unique phase property of TiO_2(B). Moreover, it should be mentioned that the morphology and structure of the materials remained unchanged after the photocatalytic reactions, as shown in Figures S1 and S2 (Supporting Information online), indicating their high stability over CO_2 photoreduction.

To verify that the carbon source of the photo-reduction products were the introduced CO_2 (reaction of $NaHCO_3$ and H_2SO_4 solution) rather than the residual carbon species that might adsorb on the surface of the reactor and the materials, $^{13}CO_2$ isotope tracer experiment was conducted. Figure 6 shows the mass spectra (MS) of the CH_4 collected after the photocatalytic conversion of $^{12}CO_2$ and $^{13}CO_2$ over TiO_2(B). The much higher intensity of the MS signal at m/z=17 ($^{13}CH_4$) compared to the signal at m/z=16 was seen when using $^{13}CO_2$ as the carbon source, demonstrating that the photocatalytic reduction products over TiO_2(B) indeed originated from the introduced CO_2 source.

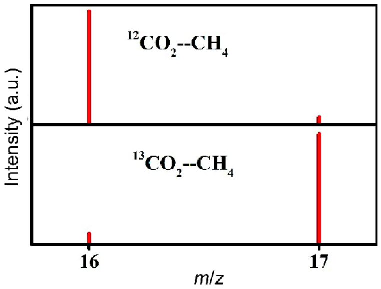

Figure 6 The MS signals of the produced CH_4 over sample TiO_2(B) using $^{12}CO_2$ and $^{13}CO_2$ as carbon source, respectively (color online).

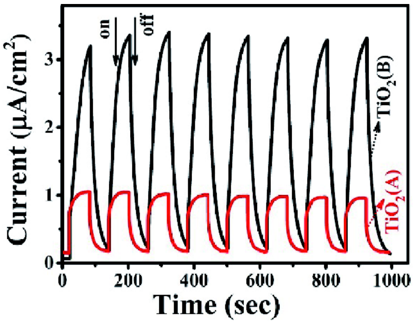

Figure 7 Transient photocurrent responses for TiO_2(B) and TiO_2(A) under LED light irradiation (λ=365 nm) in 0.5 M Na_2SO_4 aqueous solution (color online).

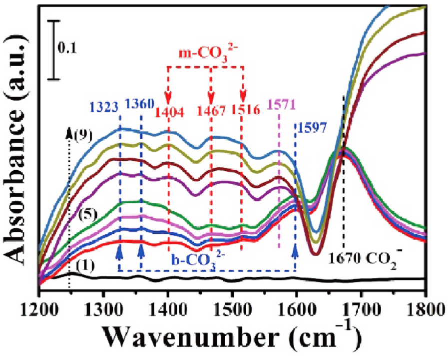

Figure 8 *In-situ* FTIR spectra of the TiO_2(B) sample: (1) without CO_2 gas in dark, (2–5) exposure to mixture of CO_2 and H_2O vapor in dark taken every 15 min interval, (6–9) exposure to mixture of CO_2 and H_2O under LED (λ=365 nm) irradiation taken every 15 min interval (color online).

3.5 Photoelectrochemical measurements

The transient photocurrents of TiO_2(B) and TiO_2(A) were measured to further study their photo-activity. The photocurrent responses were recorded by switching on and off the irradiation light for a couple of cycles (Figure 7). The TiO_2(B) exhibited the maximum photocurrent of 3.2 μA cm^{-2}, which is three times higher of TiO_2(A). This result is in good correspondence with the above-described photocatalytic CO_2 reduction activities. The gradual increase of the photocurrents indicate that the photo-generated charge carriers were first trapped by the defect states in the materials and the excess carriers could be extracted and contributed to the photocurrent. The difference in the shape of the photocurrent suggests more trap states in TiO_2(B) compared to TiO_2(A), while the slower decrease of the photocurrent of TiO_2(B) implied longer life times of charge carriers, which could be beneficial to the CO_2 photoreduction.

3.6 *In-situ* Fourier transform infrared spectroscopy

Moreover, *in-situ* Fourier transform infrared (FTIR) spectroscopy was conducted to identify the surface intermediates in the CO_2 activation and conversion process for TiO_2(B). As shown in Figure 8, the initial reactive adsorption of CO_2 mainly resulted in the formation of bidentate carbonate (b-CO_3^{2-}, at 1323, 1360 and 1597 cm^{-1}) and CO_2^- (carboxylate, 1670 cm^{-1}) as well as monodentate carbonate (m-CO_3^{2-} at 1467 and 1516 cm^{-1}) [41–48]. There was no obvious change after extended exposure to CO_2 and H_2O vapor in the dark. On the other hand, after the illumination (365 nm LED) switching on for 15 min, the peak assigned to b-CO_3^{2-} at 1597 cm^{-1} disappeared. Meanwhile, the intensities of the vibration peaks for m-CO_3^{2-} increased, especially the one at 1404 cm^{-1}. Importantly, a new adsorption peak at 1571 cm^{-1} was observed, which was attributed to the generation of formate [49,50]. The increased amount of the m-CO_3^{2-} intermediate was because the conversion of CO_2 to CO_3^{2-} is thermodynamically more favorable [7]. These observations suggest that the two carbon species of b-CO_3^{2-} and CO_2^- were the primary intermediates during the adsorption process of CO_2 and H_2O mixture on the TiO_2(B) surface. Under illumination, on the other hand, the disappearance of most b-CO_3^{2-} and the increase of m-CO_3^{2-} indicate the reactive conversion of b-CO_3^{2-} to m-CO_3^{2-} [44]. The disappearance of CO_2^- and appearance of formate indicate that illumination leads to the conversion of CO_2^- to formate. In the photocatalytic reaction process, the photo-generated electrons will transfer to the surface of the photocatalyst and reduce the adsorbed CO_2 and CO_3^{2-} to CH_4 and CH_3OH. The photo-generated hole might be captured and quenched by the surface groups (e.g., hydroxyl) [6,15].

4 Conclusions

In summary, we have successfully prepared stable monoclinic TiO_2(B) polymorph with porous hierarchical nanostructure by a microwave assisted solvothermal method combined with subsequent heat treatment in air. The as-obtained TiO_2(B) particles were constructed by ultrathin nanosheets and possessed large specific surface area, which provided many active sites for CO_2 adsorption and conversion. The samples were fully characterized by SEM, TEM, XRD, Raman, FTIR, XPS, N_2 sorption, UV-Vis and Mott-Schottky measurements. The TiO_2(B) showed a superior photocatalytic CO_2 reduction efficiency compared to anatase TiO_2 and P25. We further performed *in-situ* FTIR measurement to identify the intermediates and deduce the conversion process of CO_2 under illumination over the TiO_2(B) photocatalyst.

Acknowledgements This work was supported by the National Basic Research Program of China (2013CB632402), the National Natural Science Foundation of China (51320105001, 21433007, 51372190, 21573170), the Natural Science Foundation of Hubei Province (2015CFA001), the Fundamental Research Funds for the Central Universities (WUT: 2015-III-034), Innovative Research Funds of SKLWUT (2017-ZD-4) and the Discovery Early Career Researcher Award (DECRA) by Australian Research Council (DE160101488).

Conflict of interest The authors declare that they have no conflict of interest.

Supporting information The supporting information is available online at chem.scichina.com and link.springer.com/journal/11426. The supporting materials are published as submitted, without typesetting or editing. The responsibility for scientific accuracy and content remains entirely with the authors.

1 Ola O, Maroto-Valer MM. *J Photochem Photobiol C-PhotoChem Rev*, 2015, 24: 16–42
2 Low J, Yu J, Ho W. *J Phys Chem Lett*, 2015, 6: 4244–4251
3 Nikokavoura A, Trapalis C. *Appl Surf Sci*, 2017, 391: 149–174
4 Tu W, Zhou Y, Feng S, Xu Q, Li P, Wang X, Xiao M, Zou Z. *Chem Commun*, 2015, 51: 13354–13357
5 Marszewski M, Cao S, Yu J, Jaroniec M. *Mater Horiz*, 2015, 2: 261–278
6 Habisreutinger SN, Schmidt-Mende L, Stolarczyk JK. *Angew Chem Int Ed*, 2013, 52: 7372–7408
7 Li X, Wen J, Low J, Fang Y, Yu J. *Sci China Mater*, 2014, 57: 70–100
8 Tahir M, Tahir B, Saidina Amin NA, Alias H. *Appl Surf Sci*, 2016, 389: 46–55
9 Sim LC, Leong KH, Saravanan P, Ibrahim S. *Appl Surf Sci*, 2015, 358: 122–129
10 Inoue T, Fujishima A, Konishi S, Honda K. *Nature*, 1979, 277: 637–638
11 Low J, Cheng B, Yu J, Jaroniec M. *Energy Storage Mater*, 2016, 3: 24–35
12 Mao J, Li K, Peng T. *Catal Sci Technol*, 2013, 3: 2481–2498
13 Low J, Cheng B, Yu J. *Appl Surf Sci*, 2017, 392: 658–686
14 Dhakshinamoorthy A, Navalon S, Corma A, Garcia H. *Energy Environ Sci*, 2012, 5: 9217–9233
15 Liu L, Li Y. *Aerosol Air Qual Res*, 2014, 14: 453–469
16 Li H, Gao Y, Wu X, Lee PH, Shih K. *Appl Surf Sci*, 2017, 402: 198–207
17 Akple MS, Low J, Qin Z, Wageh S, Al-Ghamdi AA, Yu J, Liu S. *Chin J Catal*, 2015, 36: 2127–2134
18 Zhao H, Chen J, Rao G, Deng W, Li Y. *Appl Surf Sci*, 2017, 404: 49–56
19 Liu L, Zhao H, Andino JM, Li Y. *ACS Catal*, 2012, 2: 1817–1828
20 Low J, Yu J, Jaroniec M, Wageh S, Al-Ghamdi AA. *Adv Mater*, 2017, 29: 1601694
21 Yu J, Low J, Xiao W, Zhou P, Jaroniec M. *J Am Chem Soc*, 2014, 136: 8839–8842
22 Liu B, Khare A, Aydil ES. *ACS Appl Mater Interf*, 2011, 3: 4444–4450
23 Li W, Liu C, Zhou Y, Bai Y, Feng X, Yang Z, Lu L, Lu X, Chan KY. *J Phys Chem C*, 2008, 112: 20539–20545
24 Wang P, Xie T, Wang D, Dong S. *J Colloid Interf Sci*, 2010, 350: 417–420
25 Chakraborty AK, Qi Z, Chai SY, Lee C, Park SY, Jang DJ, Lee WI. *Appl Catal B-Environ*, 2010, 93: 368–375
26 Xiang G, Li T, Zhuang J, Wang X. *Chem Commun*, 2010, 46: 6801–6803
27 Ren Y, Liu Z, Pourpoint F, Armstrong AR, Grey CP, Bruce PG. *Angew Chem Int Ed*, 2012, 51: 2164–2167
28 Liu S, Jia H, Han L, Wang J, Gao P, Xu D, Yang J, Che S. *Adv Mater*, 2012, 24: 3201–3204
29 Li X, Yu J, Jaroniec M. *Chem Soc Rev*, 2016, 45: 2603–2636
30 Fu J, Zhu B, Jiang C, Cheng B, You W, Yu J. *Small*, 2017, 13: 1603938
31 Di T, Zhu B, Cheng B, Yu J, Xu J. *J Catal*, 2017, 352: 532–541
32 Jin J, He T. *Appl Surf Sci*, 2017, 394: 364–370
33 Tahir M, Tahir B. *Appl Surf Sci*, 2016, 377: 244–252
34 Chen C, Hu X, Hu P, Qiao Y, Qie L, Huang Y. *Eur J Inorg Chem*, 2013, 2013: 5320–5328
35 Akple MS, Low J, Liu S, Cheng B, Yu J, Ho W. *J CO_2 Util*, 2016, 16: 442–449
36 Xia P, Zhu B, Yu J, Cao S, Jaroniec M. *J Mater Chem A*, 2017, 5: 3230–3238
37 Wang W, Xu D, Cheng B, Yu J, Jiang C. *J Mater Chem A*, 2017, 5: 5020–5029
38 Cychosz KA, Guillet-Nicolas R, García-Martínez J, Thommes M. *Chem Soc Rev*, 2017, 46: 389–414
39 Jin J, Yu J, Guo D, Cui C, Ho W. *Small*, 2015, 11: 5262–5271
40 He Z, Tang J, Shen J, Chen J, Song S. *Appl Surf Sci*, 2016, 364: 416–427
41 Su W, Zhang J, Feng Z, Chen T, Ying P, Li C. *J Phys Chem C*, 2008, 112: 7710–7716
42 Ye L, Mao J, Peng T, Zan L, Zhang Y. *Phys Chem Chem Phys*, 2014, 16: 15675–15680
43 Collins SE, Baltanás MA, Bonivardi AL. *J Phys Chem B*, 2006, 110: 5498–5507
44 Wu W, Bhattacharyya K, Gray K, Weitz E. *J Phys Chem C*, 2013, 117: 20643–20655
45 Liu L, Jiang Y, Zhao H, Chen J, Cheng J, Yang K, Li Y. *ACS Catal*, 2016, 6: 1097–1108
46 Baltrusaitis J, Schuttlefield J, Zeitler E, Grassian VH. *Chem Eng J*, 2011, 170: 471–481
47 Mao J, Ye L, Li K, Zhang X, Liu J, Peng T, Zan L. *Appl Catal B-Environ*, 2014, 144: 855–862
48 Liao LF, Lien CF, Shieh DL, Chen MT, Lin JL. *J Phys Chem B*, 2002, 106: 11240–11245
49 Araña J, Doña-Rodrıguez JM, Cabo CG, González-Dıaz O, Herrera-Melián JA, Pérez-Peña J. *Appl Catal B-Environ*, 2004, 53: 221–232
50 Araña J, Martınez Nieto JL, Herrera Melián JA, Doña Rodrıguez JM, González Dıaz O, Pérez Peña J, Bergasa O, Alvarez C, Méndez J. *Chemosphere*, 2004, 55: 893–904